Effect of the magnetic field angle on Hall thruster plasma-wall interaction

IEPC-2022-287

Presented at the 37th International Electric Propulsion Conference
Massachusetts Institute of Technology, Cambridge, MA, USA
June 19-23, 2022

Alberto Marín-Cebrián [1], Adrián Domínguez-Vázquez [2], Pablo Fajardo [3], Eduardo Ahedo [4]
Equipo de Propulsión Espacial y Plasmas, Universidad Carlos III de Madrid, 28911 Leganés, Spain

A 1D radial Particle-In-Cell model for Hall thruster discharge has been applied to determine the effect of an oblique magnetic field into plasma fluxes at the lateral dielectric walls. The kinetic solution shows a significant replenishment of the velocity distribution function tail and subsequent temperature isotropization for scenarios in which the magnetic field deviates from normal incidence to the walls. In the radial direction, the equilibrium between the electric and pressure forces is modified by the the presence of a magnetic force, which has a confining or expanding character on electrons depending on the convexity of the magnetic lines. As a result either the density or the electric potential profiles become flat in the plasma bulk. All these changes in plasma density and temperature affect much the plasma losses to the walls. For the case of flat density profiles, the kinetic solution shows that the ion flow becomes supersonic away from the wall neighborhood. In order to explain this, a zero-Debye length fluid model is derived and analyzed. Fluid solutions show that a supersonic transition is possible away from the Debye sheath, when the radial magnetic force has a expanding character. Some parametric studies complete the paper.

I. Introduction

Most applied Hall Effect Thruster (HET) research relies on quasi-neutral fluid or hybrid PIC/fluid (for heavy species and electrons respectively) formulations since they offer a comprehensive characterization of the discharge at a low computational cost. Nonetheless, such models are not fully consistent and require to make assumptions on certain magnitudes to provide a closure to the model. In particular, it is required to define boundary conditions at the quasi-neutral sheath edge and kinetic information is required to accurately compute particle and energy losses to the wall. Additionally, non-standard effects in macroscopic transport equations may become become relevant since the electron Velocity Distribution Function (VDF) is non-Maxwellian. Alternatively, kinetic models allow to resolve the species VDF, and the macroscopic magnitudes are obtained as their corresponding velocity moments. However, they are computationally expensive and only suitable for fundamental research in simplified, low dimensional scenarios. Thus, an optimal solution would make use of these reduced kinetic results to determine approximate scaling laws for macroscopic magnitudes required for the electron fluid model. Along this line, previous works have advanced on this combined-model approach using a 1D radial kinetic model of the acceleration region of a Hall effect thruster discharge.

Considering a perfectly radial magnetic field, a recent work [1] analyzed the implications of the non-Maxwellian electron Velocity Distribution Function (VDF) on the discharge macroscopic magnitudes, transport equations and wall interaction parameters. It was found that the low plasma collisionality is insufficient to replenish the high velocity electrons collected by the walls [1–3]. This leads to a significant depletion of the radial electron VDF which has

[1]PhD candidate, Bioengineering and Aerospace engineering, almarinc@pa.uc3m.es
[2]Assistant professor, Bioengineering and Aerospace engineering, addoming@ing.uc3m.es
[3]Full professor, Bioengineering and Aerospace engineering, pfajardo@ing.uc3m.es
[4]Full professor, Bioengineering and Aerospace engineering, eahedo@ing.uc3m.es

several important implications: (*i*) induces anisotropy between radial and perpendicular electron temperatures, (*ii*) the particle and energy fluxes of electrons reaching the wall is much smaller than for a Maxwellian population, and (*iii*) non-Maxwellian VDF includes non-standard effects on macroscopic transport equations. Furthermore, significant radial asymmetries were found.

Although cases with a radial magnetic field has been widely studied in previous literature [1–5], this is typically not the case in a real scenario. Indeed, most commercial HETs feature an oblique magnetic field and many experimental studies [6, 7] have discussed on the importance of the magnetic field topology. From a theoretical perspective, plasma-wall interaction under the action of an oblique magnetic field has been extensively analyzed by the fusion plasma community [8, 9]. Nonetheless, those works assume a magnetized ion population, which is not the case here, since in HETs the typical ion Larmor radius is much larger than the thruster length. Keidar and Beilis [10] propose a simplified model of a HET plasma discharge subjected to an oblique magnetic field. Such analysis points out that the sheath magnitudes may be affected and concludes that standard boundary conditions at the sheath edge may fail in scenarios with certain magnetic field inclination. A further work by Brieda and Keidar [11] using a 2D hybrid code found that certain magnetic field configurations can protect walls from ion bombardment. State of the art electron fluid models [12–14] allow to simulate complex magnetic topologies; nonetheless, few kinetic studies analyze in detail the effects of oblique magnetic field configurations on the discharge. In this regard, Miedzik et al. [15] analyzed a HET discharge subjected to an oblique magnetic field using a 1D magnetic field aligned quasi-neutral guiding center PIC model. They discovered that scenarios with oblique magnetic field lines lead to significantly enhanced isotropization of electron temperature, even for a small departure from the normal incidence. Therefore, it questions the simplification of many kinetic models, in which the magnetic field is assumed to be perpendicular to the walls.

The current work aims to address the effect of the magnetic field angle on the plasma discharge and extend the work done in Ref. [1] to scenarios in which the magnetic field is not aligned with the radial direction. From a kinetic approach, the 1Dr model of Ref. [1] is improved to allow to simulate scenarios with an oblique magnetic field. It applies a PIC formulation for ions and electrons, accounts for secondary electron fluxes from the dielectric walls and collisions are simulated through MonteCarlo Collision (MCC) algorithms. Self-sustained stationary plasma discharge is assured by the ionization controlled discharge (ICD) algorithm of Ref. [2]. The kinetic solution is used to assess the relevant terms in the electron momentum balance and determine the effect of an oblique magnetic field on this equation. From a macroscopic approach, a simplified quasi-neutral and quasi-planar model of the plasma discharge is proposed. Fluid results are compared against PIC simulations, thus validating the model. This simplified model allows to clarify some aspects observed in kinetic results and poses questions about the the sheath edge definition, which previous works for a purely radial magnetic field [1–3] considered to be coincident with the ion sonic point position.

The article is structured as follows. Section II summarizes the main kinetic model aspects. Section III analyzes PIC simulation results for scenarios with an oblique magnetic field. The calculated electron VDF and the main macroscopic plasma magnitudes are presented. Section IV asses the importance of the different terms in the electron momentum equation. In Section V a simplified fluid model for the discharge is proposed and solved; clarifying some key aspects already observed in kinetic simulations. Particularly, it allows for the discussion the displacement of the sonic point towards the quasi-neutral plasma region in kinetic simulations under certain magnetic field configurations. Section VI focuses on the main plasma-wall interaction magnitudes and the electron power balance. Section VII discusses on the SEE model. Finally, conclusions are drawn in section VIII.

II. The kinetic radial model

The model details are briefly summarized here, highlighting the main differences with respect to previous works [1–3]. The 1D radial model (i.e. $\partial/\partial\theta = \partial/\partial z = 0$) aims to solve the plasma dynamics in an axial cross-section of an annular HET discharge, with inner and outer radii r_1 and r_2 respectively. The kinetic model applies a PIC formulation to the ion, i, and electron, e, species; simulating them as two different populations of macroparticles with constant weight (i.e. number of elementary particles per macroparticle). The VDF of ions and electrons, $f_j(t, r, \boldsymbol{v})$, $(j = i, e)$, is resolved, which allows to compute their corresponding integral moments (i.e. macroscopic magnitudes) at the radial mesh nodes. Neutrals, n, are modeled as a spatially uniform background with a time-evolving density, $n_n(t)$, and a constant temperature, T_n [2]. Collisions include $e - n$ [16–18] and Coulomb [19–22]. The Ionization Controlled Discharge (ICD), described in Ref. [2], adjusts $n_n(t)$ to keep a fixed radially-averaged plasma density $\bar{n}_e$. Such algorithm ensures an steady-state plasma discharge in which plasma volumetric production by electron-bombardment ionization balances out plasma-wall recombination. This resembles the physical conditions within the acceleration region of a HET discharge, where ionization and wall recombination tend to compensate each other [23]. Additionally, fixing the

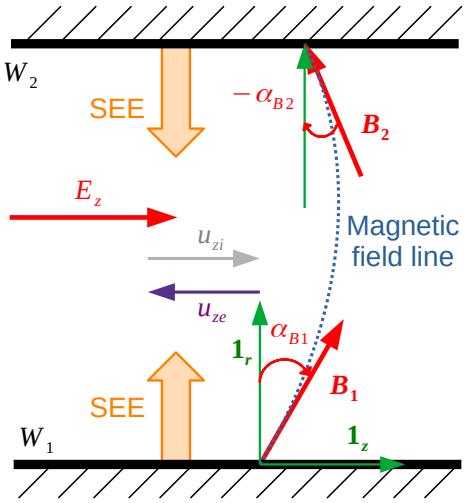

Fig. 1 Sketch of the simulation model showing: (*i*) the inner and outer walls, W_1 and W_2 respectively, (*ii*) the radial and axial versors, $\mathbf{1}_r$ and $\mathbf{1}_z$; (*iii*) secondary emission from the dielectric walls, SEE; (*iv*) the typical direction of axial electron and ion velocities, u_{ze} and u_{zi}; (*v*) the imposed axial electric field, E_z; and (*vi*) the magnetic field at the lower and upper wall, B_1 and B_2, with their respective incidence angles, α_{B1} and α_{B2}, described by a convex magnetic field line. In this sketch $\alpha_{B1} > 0$ and $\alpha_{B2} < 0$, according to the sign criterion used here.

plasma density provides a suitable framework for comparison between simulations.

The axial electric field E_z is given and the radial electric field is calculated as $E_r = -\partial\phi/\partial r$. The electric potential ϕ is obtained at the mesh nodes by solving the 1D radial Poisson equation with appropriate boundary conditions at the dielectric walls [2]. To avoid refreshing ion particles, the axial ion velocity u_{zi} is assumed constant and ions are only accelerated by E_r. A general expression for the divergence free magnetic field is given by

$$\mathbf{B}(r) = B_r(r)\mathbf{1}_r + B_z(r)\mathbf{1}_z, \qquad \text{where,} \quad B_r(r) = B_{r1}r_1/r \quad B_z(r) = B_r \tan\alpha_B, \tag{1}$$

B_r and B_z are the radial and axial magnetic field components, respectively, and α_B is the angle between the radial direction and the B-parallel direction $\mathbf{1}_\parallel = \boldsymbol{B}/B$. A right-hand orthonormal local magnetic frame $\{\mathbf{1}_\parallel, \mathbf{1}_\theta, \mathbf{1}_\top\}$ is defined with the azimuthal direction versor $\mathbf{1}_\theta$ and the $\boldsymbol{B}$-perpendicular versor $\mathbf{1}_\top = \mathbf{1}_\parallel \times \mathbf{1}_\theta$. In this low dimensional model there is not a unique way to correlate the axial and radial magnetic field components; thus, a linear variation of $\tan\alpha_B$ along the radial direction is assumed,

$$\tan\alpha_B = \frac{(r_2 - r)\tan\alpha_{B1} + (r - r_1)\tan\alpha_{B2}}{r_2 - r_1} \tag{2}$$

where α_{B1} and α_{B2} are the magnetic wall-incidence angle at the inner and outer wall respectively, as sketched in Fig. 1. Since the main objective of the current work is to study the effect of the magnetic field angle on the plasma discharge, the radially averaged magnitude of the field is kept constant for all simulations. Additionally, in order to limit the parametric space to be explored, simulations shown here consider only 'symmetric' cases for α_B (i.e. $\alpha_{B2} = -\alpha_{B1}$). Thus, according to the sign criterion used here, scenarios with convex magnetic field lines feature $\alpha_{B1} > 0$ and, for concave, $\alpha_{B1} < 0$.

In addition to plasma recombination, walls produce secondary electron emission (SEE). The SEE yield in this model follows the linear relation

$$\delta_s(\mathcal{E}_e^{(tw)}) = \mathcal{E}_e^{(tw)}/\mathcal{E}_c, \tag{3}$$

with $\mathcal{E}_e^{(tw)}$ the impacting electron energy and $\mathcal{E}_c = 51.1$ eV the material cross-over energy. The simplified law in Eq. (3) considers only true-secondary (TS) electrons (i.e. those extracted from the material surface); although more realistic models [24] also include contributions from non-true-secondary (NTS) electrons, namely backscattered

Type	Description, symbol and units	Value
Model input parameters	Mean electron density, $\bar{n}_e$ (m^{-3})	$4 \cdot 10^{17}$
	Axial ion velocity, u_{zi} (km/s)	10
Physical system parameters	Axial electric field, E_z (V/cm)	100
	Mean magnetic field, $\bar{B}$ (G)	123.5
	Inner radius, r_1 (mm)	35
	Outer radius, r_2 (mm)	50
Characteristic plasma magnitudes	Debye length, λ_D (mm)	0.03
	Larmor radius, r_L (mm)	0.80
	Inverse plasma frequency, ω_{pe}^{-1} (ps)	28
	Inverse gyrofrequency, ω_{ce}^{-1} (ps)	460
Numerical parameters	Grid spacing, Δr (mm)	0.01
	Time-step, Δt, (ps)	5
	Macroparticle weight, W	$1.5 \cdot 10^{10}$

Table 1 Reference input parameters for the 1Dr model. The characteristic plasma magnitudes are calculated taking $\bar{B} \simeq 123.5$ G, $\bar{n}_e = 4 \cdot 10^{17}$ m^{-3} and $\bar{T}_e \simeq 6.82$ eV, which corresponds to the steady-state solution for the case $\alpha_{B1} = 0$.

(elastically reflected) and rediffused (inelastically reflected) electrons. True-secondary electrons are sampled from a semi-Maxwellian VDF with an average energy of 2 eV [25]. Then, two different populations of electrons can be distinguished: primary electrons (p, bulk population) and secondary electrons (s, emitted from the walls). Here, we consider that s are transferred to p due to collisions, following the same criterion as in Ref. [1].

Finally, quasi-planar geometries can be simulated with the code by including an offset distance r_o to the simulation domain. A planar configuration corresponds to $r_o \gg r_2 - r_1$. Planar simulations presented here take $r_o = 1$ km.

III. Kinetic results

For all simulations shown here, xenon is the propellant. The main model input parameters are summarized in Table 1. A uniform radial mesh with a cell size smaller than the Debye length is chosen. Accurate integration of particle trajectories is ensured by setting the simulation time-step $\Delta t = 5$ ps $< 0.3\omega_{pe}^{-1}$; where ω_{pe} is the plasma frequency, which is larger than the gyrofrequency ω_{ce} in all simulations. The total simulation time is 9 μs and the steady-state results shown here are time averages of the last microsecond. The macroparticle weight, has been selected such that there are $\sim 10^5$ simulated particles per species, yielding a good compromise between computational time and accuracy [1–3]. Simulations start with full Maxwellian distributions at $T_{e0} = 10$ eV and $T_{i0} = 1$ eV for electrons and ions respectively, and identical particle densities $n_{e0} = n_{i0} = 4 \cdot 10^{17}$ m^{-3}, which evolve in time until reaching its stationary solution. Steady-state macroscopic magnitudes are obtained using the Extended Volumetric Weighting [2] algorithm. A bar over a magnitude indicates that it is a radially averaged value, such that

$$\bar{\Phi} = \frac{2}{r_2^2 - r_1^2} \int_{r_1}^{r_2} \Phi(r) r \mathrm{d}r, \tag{4}$$

where $\Phi(r)$ is any given radial profile.

In this section, kinetic simulations of the annular HET channel with $\alpha_{B1} = -15$, 0 and 15 deg. are described first in terms of the electron VDF and then based on macroscopic profiles and parameters.

A. The electron VDF

Fig. 2 depicts the 1D normalized electron VDF along the $\boldsymbol{B}$-parallel and $\boldsymbol{B}$-perpendicular directions at mid-radius M

$$\hat{f}_e^{(\parallel)}(v_\parallel) \propto \int_{-\infty}^{\infty} \int_{-\infty}^{\infty} f_e(\boldsymbol{v}) \mathrm{d}v_\theta \mathrm{d}v_\top, \tag{5a}$$

Magetic field angle (deg)	α_{B1}	-15	0	15
Ionization frequency (10^3 s^{-1})	$\bar{\nu}_{prod}$	77	166	333
Axial electron current (A/m^2)	$\bar{j}_{ze}$	47.4	89.9	241.5
Radially averaged electron temperatures (eV)	$\bar{T}_{re}$	6.58	4.93	6.12
	$\bar{T}_{\theta e} \simeq \bar{T}_{ze}$	7.07	7.76	6.49
Electric potential (V)	ϕ_M	29.1	19.6	36.5
Non-dimensional sheath potential drop ($-$)	$e\phi_{WQ_1}/T_{eQ1}$	3.66	2.14	3.85
	$e\phi_{WQ_2}/T_{eQ2}$	3.79	1.97	3.82
Replenishment factor ($-$)	σ_{rp1}	0.28	0.06	0.49
	σ_{rp2}	0.33	0.07	0.50
Energy ratio ($-$)	Θ_1	0.74	0.66	0.79
	Θ_2	0.82	1.01	0.85
SEE yield ($-$)	δ_{s1}	0.21	0.16	0.21
	δ_{s2}	0.25	0.32	0.26
Electron current densities towards the walls (A/m^2)	$\lvert j_{e1}^{(tw)}\rvert$	41	81	196
	$\lvert j_{e2}^{(tw)}\rvert$	54	131	220

Table 2 Main parameters characterizing the steady-state plasma discharge. For all these simulations $\phi_{W_2} = 0$ and ϕ_{W_1} ranges from 1.3 to 2.3 V.

$$\hat{f}_e^{(\top)}(v_\top) \propto \int_{-\infty}^{\infty}\int_{-\infty}^{\infty} f_e(\boldsymbol{v})\mathrm{d}v_\parallel \mathrm{d}v_\theta, \tag{5b}$$

and they are compared with a Maxwellian VDF at the corresponding electron temperature at M for each case, T_{eM}. Since $\alpha_B(r)$ is symmetric; then, $\alpha_B(r_M) = 0$, yielding $v_\parallel \equiv v_r$ and $v_\top \equiv v_z$ in these figures and for that specific location.

For the three angles, $\hat{f}_e^{(\top)}(v_\top)$ is approximately Maxwellian, while $\hat{f}_e^{(\parallel)}(v_\parallel)$ is Maxwellian-like for small velocities but presents partially-depleted high velocity tails. The depletion level and, therefore, the temperature anisotropy are maximum for $\alpha_{B1} = 0$. This suggests that oblique magnetic incidence allows a larger transfer or electrons between v_r and v_z regions.

The resulting VDFs are not symmetric for convex ($\alpha_{B1} > 0$) and concave ($\alpha_{B1} < 0$) magnetic configurations: for instance, scenarios with $\alpha_{B1} > 0$ feature a lower T_e and the replenishment fraction (commented in Section VI) is different too. The vertical lines in Fig. 2 are just estimating which regions of $\hat{f}_e^{(\parallel)}(v_\parallel)$ correspond to electrons that can be collected at one of the walls. Disregarding the effect of magnetic mirror and cylindrical expansion terms, the

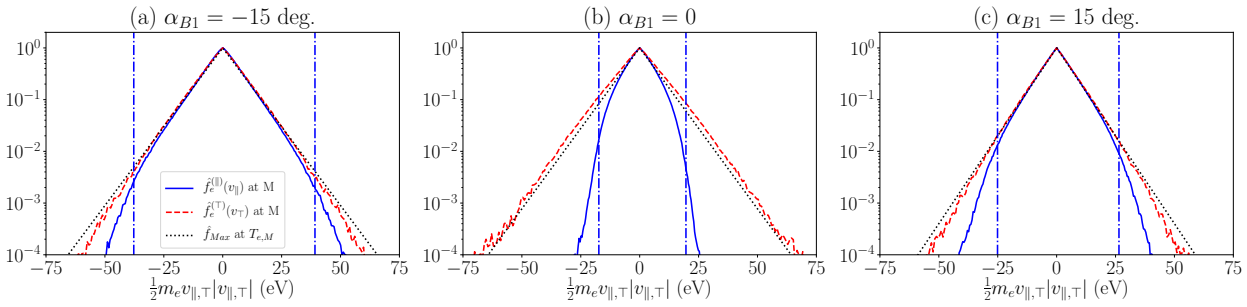

Fig. 2 1D parallel (solid, blue) and perpendicular (dashed, red) VDFs [see Eq. (5)] at M, together with a Maxwellian VDF with T_{eM} (dotted, black). The vertical lines show the approximate wall collection energy.

$\boldsymbol{B}$-parallel gyrocenter electron energy satisfies

$$\frac{1}{2}m_e(v_{\parallel M}^2 - v_{\parallel W}^2) \simeq e(\phi_M - \phi_W) - eE_z \int_{r_M}^{r_W} \tan\alpha_B \mathrm{d}r \tag{6}$$

Setting $v_{\parallel W} = 0$ at W_1 and W_2, we obtain for $m_e v_{\parallel M}^2/2$ the vertical dashed lines of Fig. 2.

B. Macroscopic magnitudes

All the ion and electron macroscopic magnitudes presented hereafter are obtained by taking velocity moments of their VDF at the final steady-state. Fig. 3 depicts radial profiles of main plasma magnitudes and Table 2 gathers the main parameters characterizing the discharge at steady-state conditions.

For all the simulations reported here, $\bar{n}_s \ll \bar{n}_e$; thus, s electrons do not play an important role shaping the profiles of the main plasma magnitudes. The ICD algorithm calculates the required neutral density to keep a constant $\bar{n}_e$. The required n_n to achieve a stationary discharge grows with α_{B1}. This enhances $e-n$ collisions and ionization, as shown in Table 2. In the final steady state, plasma production and wall losses must balance. As a consequence, the growing trend of $\bar{\nu}_{prod}$ with α_{B1} suggest an increase in particle fluxes to the wall. This is confirmed by the computed electron currents to the walls in Table 2. Plasma-wall interaction magnitudes are further commented in Section VI.

Radially averaged temperatures in the cylindrical reference frame are gathered in Table 2 and confirm the aforementioned reduction in anisotropy that can be observed in the electron VDF in Fig. 2 for scenarios with an oblique magnetic field. Electron temperature isotropization under oblique magnetic field configurations was previously found by Miedzik in Ref. [15]. The total electron temperature profile is depicted in Fig. 3(d). This magnitude does not exhibit significant radial variations in the domain and it is weakly affected by α_{B1}; although, higher temperatures are obtained for $\alpha_{B1} = -15$ deg. and lower for $\alpha_{B1} = 15$ deg.

The ion radial macroscopic velocity, u_{ri}, normalized with the local sound speed, $c_s = \sqrt{T_e/m_i}$, is shown in Fig.

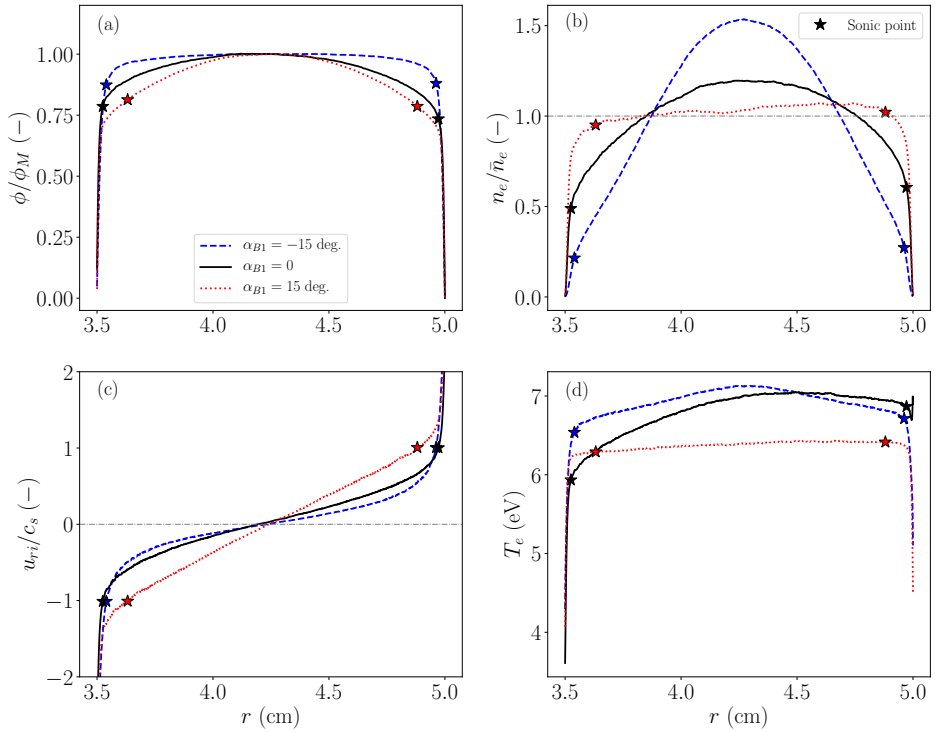

Fig. 3 Macroscopic radial profiles, for $\alpha_{B1} = -15$, 0 and 15 deg., of (a) the electric potential, ϕ, normalized with ϕ_M; (b) the electron density, n_e, normalized with its mean value, $\bar{n}_e$; (c) the radial ion velocity, u_{ri}, normalized with the local sound speed, c_s; and (d) the electron temperature T_e. Star markers indicate the sonic transition $u_{ri}/c_s = 1$.

3(c). As expected, simulations with $\alpha_{B1} = -15$ deg. and $\alpha_{B1} = 0$ present an abrupt subsonic to supersonic transition close to the walls in a region with strong gradients of u_{ri}/c_s. Nonetheless, for $\alpha_{B1} = 15$ deg., the position at which ions become sonic moves inwards the channel and the supersonic transition is regular. Furthermore, Fig. 3(c) shows that u_{ri}/c_s is approximately linear with r for $\alpha_{B1} = 15$ deg. Further discussion about this topic and an explanatory simplified fluid model can be found in Section V.

The electric potential at M can be found in Table 2; while its radial profile, ϕ/ϕ_M is depicted in 3(a). The radial profile of ϕ is almost flat for $\alpha_{B1} = -15$ deg. (excluding the sheath region) but for $\alpha_{B1} = 15$ deg. radial gradients increase. On the other hand, the electron density profile, $n_e/\bar{n}_e$ in Fig. 3(b), is rather uniform in the plasma bulk region for $\alpha_{B1} = 15$ deg., whereas significant radial variations can be found for $\alpha_{B1} = -15$ deg. In order to explain this behavior, the electron momentum equation is analyzed in Section IV.

IV. Analysis of the electron momentum equation

At steady-state, the kinetic solution for electrons is found to fulfill the macroscopic momentum equation [1]

$$\mathbf{0} = -\nabla \cdot \bar{\bar{M}} - en_e(\boldsymbol{E} + \boldsymbol{u}_e \times \boldsymbol{B}) + \boldsymbol{F}_{col}, \tag{7}$$

where $\boldsymbol{u}_e$ is the macroscopic electron velocity, $\boldsymbol{F}_{col}$ is the force due to collisions, and

$$\bar{\bar{M}} = m_e \int \boldsymbol{v}\boldsymbol{v} f_e(\boldsymbol{v}) d\boldsymbol{v} \equiv \bar{\bar{U}} + \bar{\bar{P}} \tag{8}$$

is the (symmetric) momentum flux tensor for electrons, sum of the momentum convection tensor, $\bar{\bar{U}} = m_e n_e \boldsymbol{u}_e \boldsymbol{u}_e$, and the pressure tensor $\bar{\bar{P}} = m_e \int \boldsymbol{c}\boldsymbol{c} f_e(\boldsymbol{v}) d\boldsymbol{v}$, with $\boldsymbol{c} = \boldsymbol{v} - \boldsymbol{u}_e$ the thermal velocity. All terms in Eq. (7) can be computed from the kinetic solution.

For normal magnetic incidence $\bar{\bar{P}}$ is easily expressed as a gyrotropic (diagonal) part, featuring parallel and perpendicular pressures, and a gyroviscous (non-diagonal) part, whose terms are $O(10^{-2})$ typically, compared to diagonal ones. For oblique magnetic incidence, the gyrotropic/gyroviscous separation is still valid in a magnetically aligned frame, but a rotation must be applied to express $\bar{\bar{P}}$ in the preferred cylindrical reference frame. Simulations for $|\alpha_{B1}| \leq 30$ deg show that, in the cylindrical frame, the non-diagonal part continues to be of order $O(10^{-2})$ compared to the diagonal part.

Along the axial direction, the strong electric and magnetic forces keep dominating over $(\nabla \cdot \bar{\bar{M}})_z$ and $F_{z,col}$. Thus, the axial momentum equation continues yielding with good approximation

$$u_{\theta e} \simeq E_z/B_r. \tag{9}$$

The azimuthal momentum equation is

$$j_{ze} \cos\alpha_B - j_{re} \sin\alpha_B = \frac{1}{B}\left[(\nabla \cdot \bar{\bar{M}})_\theta - F_{\theta,col}\right]. \tag{10}$$

with the new term proportional to j_{re} for oblique incidence. This radial current changes sign at the channel center and becomes of the order of j_{ze} near the walls, as shown in Table 2. Therefore, its influence on the above equation is mainly local and felt only for $|\tan\alpha_{B1}| \geq 1$. Its sign depend on that of α_{B1}, e.g. it enforces j_{ze} for $\alpha_{B1} > 0$. The integration of Eq. (10) allows to determine I_{ze}. There the influence of j_{re}-term is small, of the same order of the gyroviscous contribution for simulations with $|\alpha_{B1}| \leq 30$ deg. and I_{ze} is dominated by the collisional term. A deeper analysis of Eq. (10) can be found in Ref. [1] for a purely radial magnetic field and, apart from the differences highlighted previously, it continues to be valid in simulations with an oblique magnetic field.

The main novelties for oblique incidence are found in the radial momentum equation, which reads

$$0 \simeq -(\nabla \cdot \bar{\bar{M}})_r + en_e \frac{\partial\phi}{\partial r} + B_z j_{\theta e}. \tag{11}$$

Using Eq. (9), the radial magnetic force can be expressed as

$$B_z j_{\theta e} \simeq -en_e E_z \tan\alpha_B. \tag{12}$$

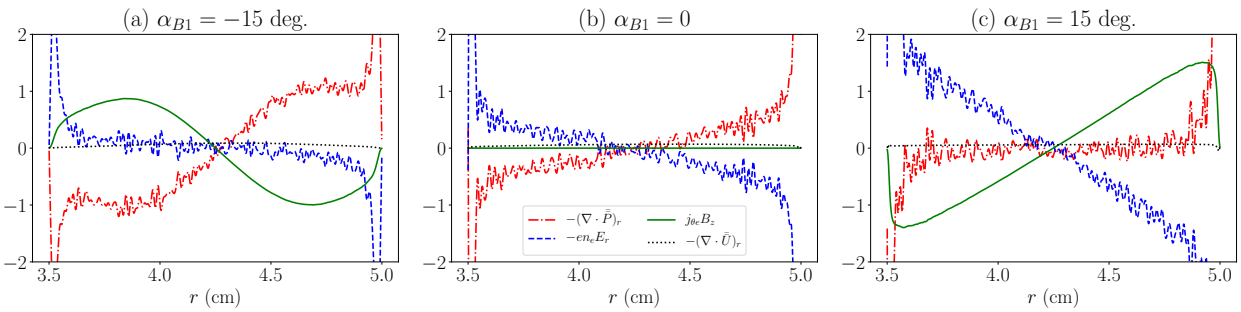

Fig. 4 Individual contributions to Eq. (11), radial momentum, in Pa/cm, for $\alpha_{B1} = -15$, 0 and 15 deg.

The momentum flux term satisfies[1]

$$(\nabla \cdot \bar{\bar{M}})_r = (\nabla \cdot \bar{\bar{P}})_r + (\nabla \cdot \bar{\bar{U}})_r, \qquad \text{where:} \quad (\nabla \cdot \bar{\bar{P}})_r \simeq \frac{\partial n_e T_{re}}{\partial r} + \frac{n_e}{r}\left(T_{re} - T_{\theta e}\right), \quad (\nabla \cdot \bar{\bar{U}})_r \simeq -\frac{n_e}{r} m_e u_{\theta e}^2, \tag{13}$$

where the terms proportional to $1/r$ introduce cylindrical effects due to anisotropy and azimuthal electron drift.

The electron inertia tends to be much smaller than the other contributors to the radial electron momentum. Thus, Eq. (11) expresses a balance among pressure, electric, and magnetic forces. Typically, the pressure force is an outwards (i.e. expanding) one, and the electric force is an inwards (i.e. confining) one. Instead, the magnetic force changes sign with α_{B1}, so it is an outwards one for $\alpha_{B1} > 0$ and inwards one for $\alpha_{B1} < 0$. This is going to explain the different force balances we find for positive and negative magnetic incidences. Furthermore, for the cases considered here, in the bulk plasma region $E_z \gg |\partial\phi/\partial r|$, so small values of α_{B1} are going to imply a large change in that balance. Fig. 4 plots the different contributions to Eq. (11) for 3 magnetic incidences, $\alpha_{B1} = -15$, 0, and 15 degrees. For $\alpha_{B1} = 0$, the electric and pressure forces balance each other. For $\alpha_{B1} = -15$ deg., the electric force is small and confinement is achieved mostly by the magnetic force, which opposes to the electron pressure; this is in line with the near-flat potential profile of Fig. 3(a). For $\alpha_{B1} = 15$ deg, on the contrary, the pressure force has become marginal and the magnetic force is alone trying to expand the electron fluid; this is now in line with the near-flat density profile of Fig. 3 (b).

To understand better the coupled plasma response, we propose and analyze next a simple fluid model which keeps the essential fluid dynamic aspects of the discharge. Furthermore, it will also provide answers to why the ion sonic point seems to move inwards the plasma bulk for α_{B1} positive in Fig. 3(c).

V. Simple fluid model

The fluid model assumes: (*i*) steady-state, (*ii*) quasi-neutrality, (*iii*) cold ions, (*iv*) a uniform and isotropic electron temperature, (*v*) constant production frequency, and (*vi*) neglects cylindrical effects. Under these hypotheses, the plasma is described by the following set of equations

$$\frac{\mathrm{d}}{\mathrm{d}r}(n_e u_{ri}) = n_e \bar{\nu}_{prod}, \tag{14}$$

$$m_i \frac{\mathrm{d}}{\mathrm{d}r}(n_e u_{ri}^2) = -e n_e \frac{\mathrm{d}\phi}{\mathrm{d}r}, \tag{15}$$

$$0 = e n_e \frac{\mathrm{d}\phi}{\mathrm{d}r} - \bar{T}_e \frac{\mathrm{d}n_e}{\mathrm{d}r} - e n_e E_z \tan\alpha_B, \tag{16}$$

for the unknowns n_e, u_{ri}, and ϕ.

Calling $d = r_2 - r_M$ the half-channel width and $\bar{c}_s = \sqrt{\bar{T}_e/m_i}$ the (mean) sound speed; the following dimensionless variables are defined,

$$\zeta = \frac{r - r_M}{d}, \quad \hat{u}_{ri} = \frac{u_{ri}}{\bar{c}_s}, \quad \hat{n}_e = \frac{n_e}{n_{eM}}, \quad \hat{\phi} = \frac{e(\phi - \phi_M)}{\bar{T}_e}, \tag{17}$$

and parameters

$$\hat{\nu}_{prod} = \bar{\nu}_{prod}\frac{d}{\bar{c}_s}, \quad F = \frac{eE_z}{\bar{T}_e}\frac{d}{2}\tan\alpha_{B1}. \tag{18}$$

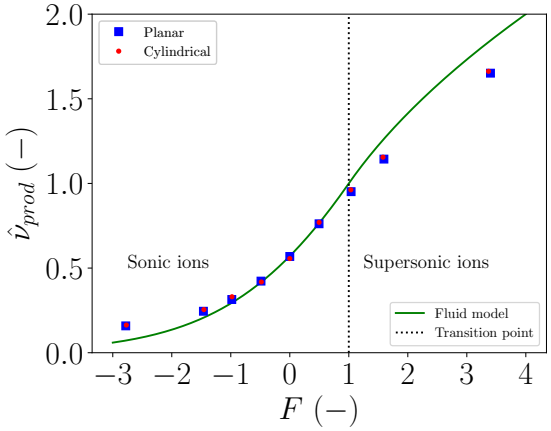

Fig. 5 Plasma production $\hat{\nu}_{prod}$ versus radial magnetic force F in the simple fluid model. For $F > 1$, $\hat{\nu}_{prod} = \sqrt{F}$. Markers correspond to the exact kinetic solutions; from left to right, simulations feature $\alpha_{B1} = -30$, -15, -10, -5, 0, 5, 10 and 30 deg.

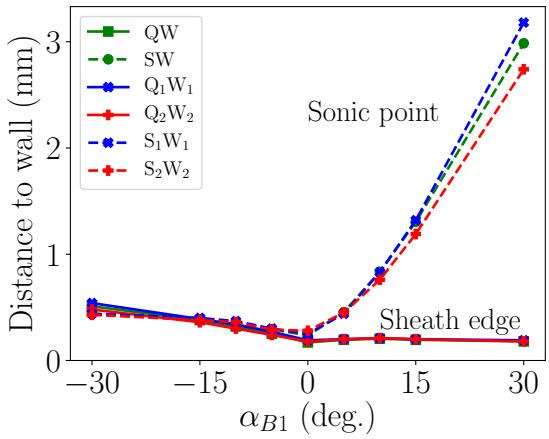

Fig. 6 Distance to adjoining walls W_1 and W_2 of the sonic points, S_1 and S_2 (dashed lines), and sheath edges, Q_1 and Q_2 (solid lines), obtained from the exact kinetic solution. Results without subscript correspond to planar cases.

Then, solving for $\mathrm{d}\hat{u}_{ri}/\mathrm{d}\zeta$ one has

$$(1-\hat{u}_{ri}^2)\frac{\mathrm{d}\hat{u}_{ri}}{\mathrm{d}\zeta} = \hat{\nu}_{prod}(1+\hat{u}_{ri}^2) - 2\hat{u}_{ri}F\zeta. \tag{19}$$

Here: we impose $\hat{u}_{ri} = 0$ at $\zeta = 0$; F measures the magnetic force contribution, which changes sign with α_{B1}; and $\hat{\nu}_{prod}$ is an eigenvalue of the model, to be determined, in the zero Debye length limit, by the boundary condition at the non-neutral sheath transition at $\zeta = 1$.

Since Eq. (19) is singular at the sonic point $\hat{u}_{ri} = 1$, we impose this to be the boundary condition at $\zeta = 1$, i.e. the sheath transition is assumed sonic. This condition yields a valid numerical solution of Eq. (19) for all $F \leq 1$ (including all negative values). The corresponding values of $\hat{\nu}_{prod}(F)$ are plotted in Fig. 5 and indicate a monotonic behavior. For F negative, the larger is $|F|$, the lower is the production frequency $\hat{\nu}_{prod}$ (i.e. the neutral density) required to establish a stationary solution (with given $\bar{n}_e$). This agrees very exactly with the behavior observed in the kinetic solution and is clearly illustrated by the square and circle markers of Figure 5 (for kinetic solutions in planar and cylindrical geometries respectively).

In the parametric region $F \leq 1$, Eq. (19) has no simple analytical solution, but an expansion around $\zeta = 0$ yields

$$\begin{aligned}
\hat{u}_{ri} &\simeq \hat{\nu}_{prod}\zeta\left[1+\frac{2}{3}(\hat{\nu}_{prod}^2 - F)\zeta^2\right] + O(\zeta^5),\\
\hat{n}_e &\simeq 1 - (\hat{\nu}_{prod}^2 - F)\zeta^2 + O(\zeta^4),\\
\hat{\phi} &\simeq -\hat{\nu}_{prod}^2\zeta^2 + O(\zeta^4).
\end{aligned} \tag{20}$$

These trends coincide with those plotted in Fig. 3. For F negative, $\hat{\nu}_{prod}$ is small and $\hat{\nu}_{prod}^2 - F \simeq |F|$, the gradient of $\hat{u}_{ri}$ is small, and $\hat{\phi}$ becomes very flat.

For the range $F > 1$, the sonic condition $\hat{u}_{ri}(1) = 1$ cannot be satisfied. Instead, there exists a regular sonic transition for

$$\hat{\nu}_{prod} = \sqrt{F}; \tag{21}$$

and then, the fluid solution is surprisingly simple

$$\hat{u}_{ri}(\zeta) = \sqrt{F}\,\zeta, \qquad \hat{n}_e = 1, \qquad \hat{\phi} = -F\zeta^2. \tag{22}$$

This solution states that: (*i*) the ion flow enters the Debye sheath (at $\zeta \simeq 1$), with a supersonic velocity, as already suggested by PIC results in Fig. 3(c); and (*ii*) there are not pressure gradients for $F > 1$, in agreement with the kinetic results in Fig. 4(c).

The Bohm criterion asserts that the establishment of a Debye sheath requires sonic or supersonic entrance conditions. However, there are not many physical situations where a supersonic sheath transition applies to a quasi-neutral flow starting from rest, like in the present case. In order to confirm this behavior, it is required to determine the location of the ion sonic point and the the sheath transition from the kinetic solution at different magnetic angles. These locations are approximate since there are not exact definitions for the two of them in the kinetic model. Near each wall, the ion sonic point S was defined as $|u_{ri}| = c_s$ and we define the sheath transition point Q as the one with

$$|n_{iQ} - n_{eQ}|/n_{iQ} = 0.05. \tag{23}$$

Figure 6 plots the locations of these points, relative to their adjoining wall. As anticipated by the simple fluid model and considering the small arbitrariness of the definitions, both points can be considered the same for $\alpha_{B1} \leq 0$, whereas the sonic point moves significantly into the quasineutral region for $\alpha_{B1} > 0$. It is also worth observing that the sheath thickness is constant for $\alpha_{B1} > 0$ and increases with $|\alpha_{B1}|$ for negative magnetic angles. Since the sheath thickness is proportional to the Debye length, we are just observing the effect of the different values of n_e at the sheath edge with α_{B1}.

Figure 7 compares radial profiles of the main plasma magnitudes obtained from the fluid and PIC results (in

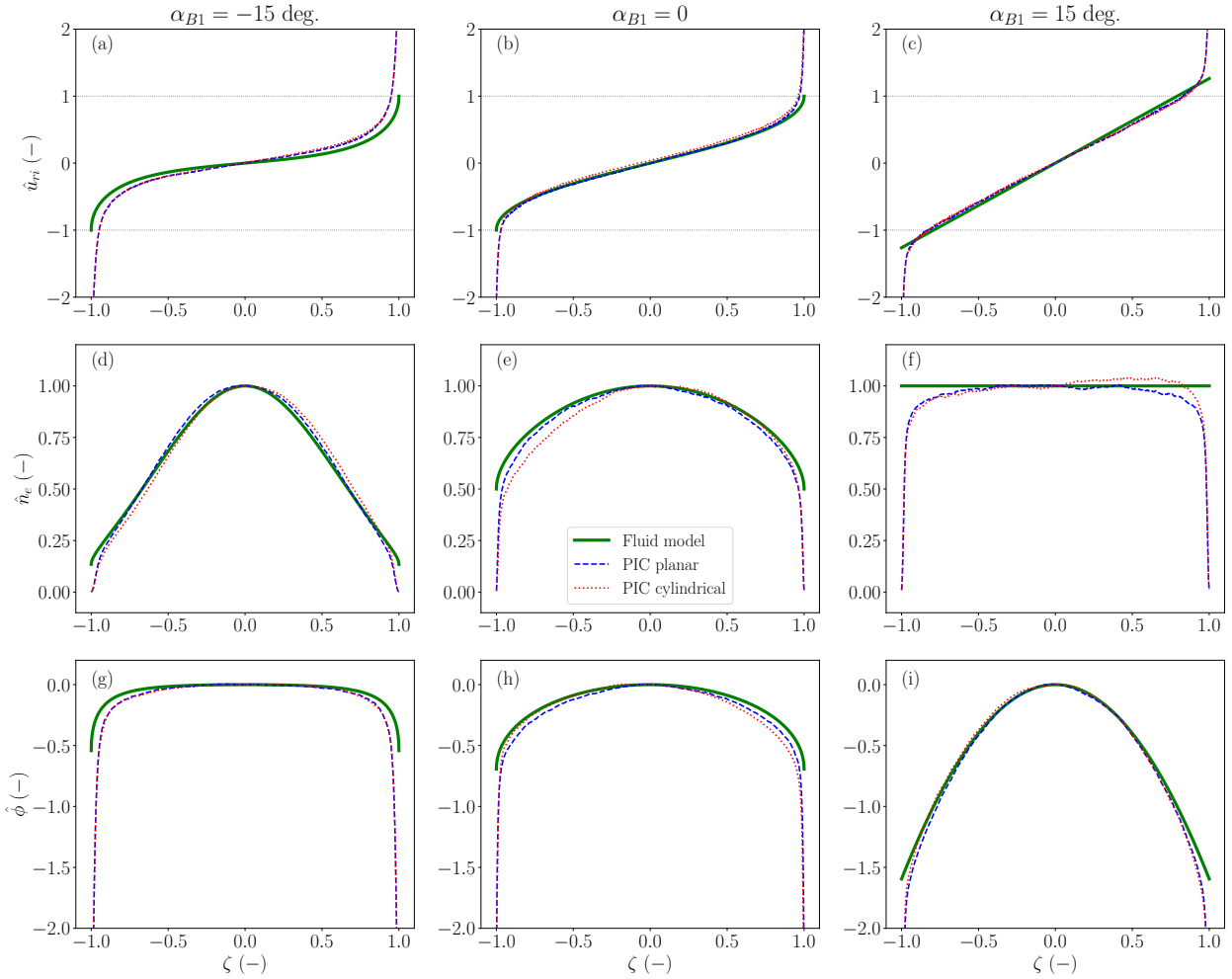

Fig. 7 Comparison between fluid and PIC solutions for $\alpha_{B1} = -15, 0, 15$ deg in terms of non-dimensional ion velocity $\hat{u}_{ri}$, (a), (b) and (c); electron density $\hat{n}_e$, (d), (e) and (f); and electric potential $\hat{\phi}$, (g), (h) and (i).

cylindrical and planar configurations). The fluid model is capable of accurately reproducing the bulk plasma behavior computed from the kinetic solution, further validating the fluid solution. The main differences are located in the vicinity of the walls since the quasi-neutral model can not resolve the non-neutral Debye sheaths.

VI. Wall interaction parameters and contributions to electron energy

As Table 2 illustrates, plasma-wall interaction magnitudes are significantly affected by the magnetic incidence angle. In this work, as in Ref. [1], we are interested in assessing key parameters of that interaction which can be applicable to two-scale plasma models, where the Debye sheaths are treated as electrostatic discontinuities.

Let us start with the ions impacting a wall W. Calling $\phi_{WQ} = \phi_Q - \phi_W$ the potential fall across the sheath; the ion current density, $|j_i^{(tw)}|$, and average impact energy per ion, $\langle \mathcal{E}_i^{(tw)} \rangle$, computed from the kinetic solution satisfy

$$|j_i^{(tw)}| \simeq e n_{iQ} u_{riQ}, \tag{24}$$

$$\langle \mathcal{E}_i^{(tw)} \rangle \simeq \frac{1}{2} m_i u_{iQ}^2 + e\phi_{WQ}; \tag{25}$$

with errors below 1% and 3%, in Eqs. (24) and (25), respectively.

The electron current density *towards* wall W is expressed relative to the flux for a Maxwellian electron population as[1]

$$|j_e^{(tw)}| = \sigma_{rp} \cdot e n_{eQ} \exp\left(-\frac{e\phi_{WQ}}{T_{eQ}}\right) \sqrt{\frac{T_{eQ}}{2\pi m_e}}. \tag{26}$$

This formula defines σ_{rp}, which measures the replenishment fraction of the electron VDF. Then, the average impact energy per electron is per electron is

$$\langle \mathcal{E}_e^{(tw)} \rangle = \Theta \cdot (2T_{eQ} + m_e u_{\theta eQ}^2/2), \tag{27}$$

which defines Θ, the ratio of that energy versus the one for a drifted-Maxwellian population[1]. Θ is in the range $0.65 - 1$, with lower values at the inner wall and perpendicular magnetic incidence. It is consistently higher at W_2 but asymmetries are lower for oblique magnetic fields.

Regarding σ_{rp}, it experiences a significant growth in scenarios with $\alpha_{B1} \neq 0$. This is in agreement with the lower anisotropy and higher VDF replenishment for oblique magnetic fields observed in Table 2 and Fig. 2. Simulations with $\alpha_{B1} > 0$ have higher σ_{rp} than their negative counterparts. According to Eq. (6), for $\alpha_{B1} < 0$, the oblique magnetic field has the effect of preventing the electron motion towards the walls, and the opposite happens for $\alpha_{B1} > 0$. Therefore, it is easier for an electron located at the sheath edge to reach the wall if $\alpha_{B1} > 0$.

The electron current density *from* wall W can be expressed as

$$|j_e^{(fw)}| = \langle \delta_s \rangle \cdot |j_e^{(tw)}| \tag{28}$$

where $\langle \delta_s \rangle$ is the effective (or global) SEE yield, detailed in Table 2. According to Eq. (3), δ_s is low (ranging from $0.16 - 0.33$) due to the low energy of impinging electrons on the wall.

The zero net current condition at the dielectric wall imposes $|j_i^{(tw)}| = |j_e^{(tw)}| - |j_e^{(fw)}|$. Table 2 shows that particle fluxes to the wall are higher for increasing values of α_{B1}. Changes in such magnitudes are mainly driven by those in n_e and u_{ri} near the wall in Fig 3(b) and (c).

Combining Eqs. (24), (26) and (28) together with the zero current condition, the different sheath-related parameters satisfy

$$\frac{e\phi_{WQ}}{T_{eQ}} \simeq \ln \sqrt{\frac{m_i}{2\pi m_e}} - \ln \frac{u_{riQ}/c_{sQ}}{\sigma_{rp}(1 - \langle \delta_s \rangle)}. \tag{29}$$

with $u_{riQ}/c_{sQ} \geq 1$ the ion radial Mach number at the sheath edge. The first term of the right side of Eq. (29) is 5.27 for Xe, increasing values of u_{riQ}/c_{sQ}, and $\langle \delta_s \rangle$, together with low σ_{rp} decrease the relative potential drop. The values of $e\phi_{WQ}/T_{eQ}$ are summarized in Table 2. In the present simulations, the main influence is due to the replenishment fraction and make $e\phi_{WQ}/T_{eQ}$ range from 2 to 4, with a minimum value for $\alpha_{B1} = 0$.

The energy losses of electrons to the wall are part of the global electron energy balance, which reads [1]

$$\mathcal{P}_{E_z} = |\mathcal{P}_{E_r}| + |\mathcal{P}_{wall}| + |\mathcal{P}_{col}| \tag{30}$$

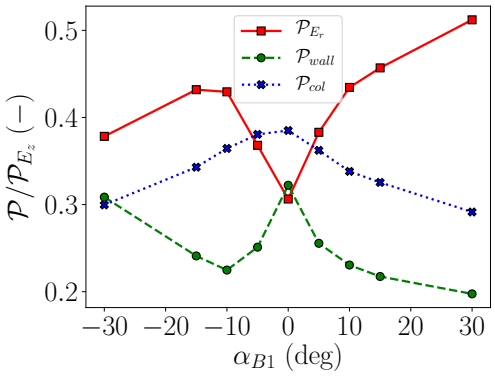

Fig. 8 Relative contributions to the electron power balance as a function of α_{B1}.

where the only energy source $\mathcal{P}_{E_z} = I_{ze}E_z$ is spent among: the work of the radial electric field, $|\mathcal{P}_{E_r}|$; the electron losses to the wall, $|\mathcal{P}_{wall}|$; and the losses due to inelastic collisions, $|\mathcal{P}_{col}|$. All the terms in this balance increase with α_{B1}. The effect of α_{B1} in $\mathcal{P}_{E_z}$ is felt through $I_{ze} = \pi\left(r_2^2 - r_1^2\right)\bar{j}_{ze}$, listed in Table 2. The relative distribution of $\mathcal{P}_{E_z}$ among the three other terms, changes mildly with the magnetic angle, as shown in Fig. 8.

VII. On the secondary electron emission model

This section is devoted to analyze the the effect of the secondary electron emission model on the simulation results. The reference simulation makes use of the SEE model proposed in Section II, which is compared against the more

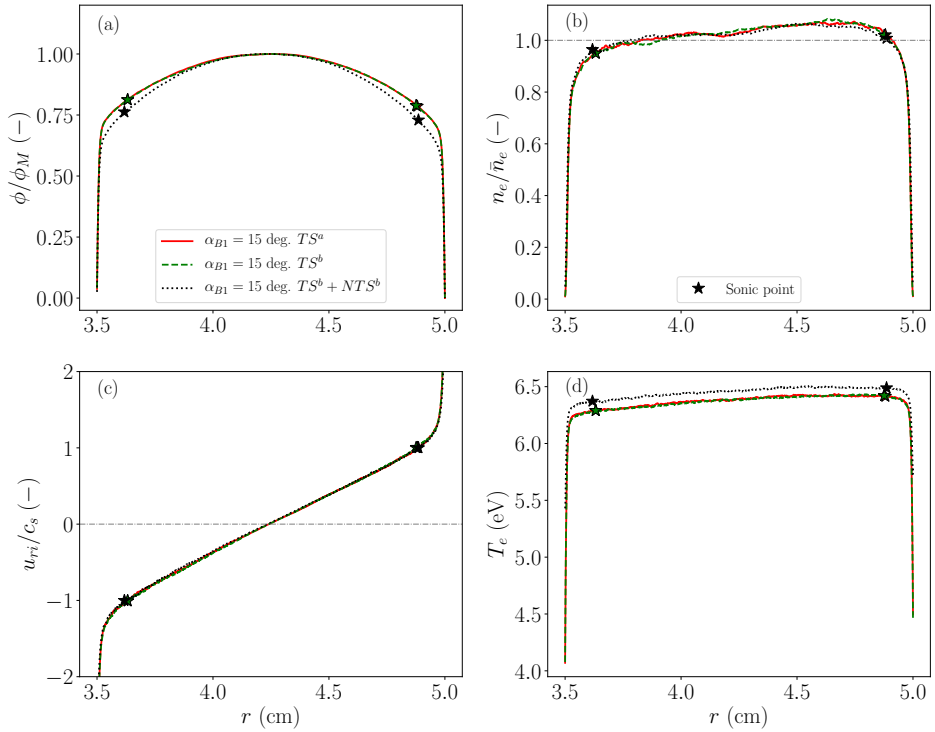

Fig. 9 Radial profiles of relevant macroscopic magnitudes for different SEE models and $\alpha_{B1} = 15$ deg. The different SEE models to be compared are identified by the superscript over the secondary electron types considered for the simulation: a corresponds to the SEE model defined in Section II and b uses the SEE model from Ref. [24].

Secondary electrons	Types	TS^a	TS^b	$TS^b + NTS^b$
Radially averaged electron temperatures (eV)	$\bar{T}_{re}$	6.12	6.12	6.18
	$\bar{T}_{\theta e} \simeq \bar{T}_{ze}$	6.49	6.49	6.59
Electron impact energy (−)	$\langle \mathcal{E}_{e1}^{(tw)} \rangle$	10.76	10.92	13.81
	$\langle \mathcal{E}_{e2}^{(tw)} \rangle$	13.00	13.04	14.63
Secondary electron emission energy (−)	$\langle \mathcal{E}_{e1}^{(fw)} \rangle$	2.01	2.01	8.42
	$\langle \mathcal{E}_{e2}^{(fw)} \rangle$	2.00	2.01	8.78
SEE yield (−)	$\langle \delta_{s1} \rangle$	0.21	0.20	0.83
	$\langle \delta_{s2} \rangle$	0.26	0.24	0.85
Replenishment factor (−)	σ_{rp1}	0.49	0.49	0.78
	σ_{rp2}	0.50	0.50	0.76
Energy ratio (−)	Θ_1	0.79	0.80	1.00
	Θ_2	0.85	0.86	0.95
Eelectric potential (V)	ϕ_M	36.51	36.67	29.47
Non-dimensional sheath potential drop (−)	$e\phi_{WQ_1}/T_{eQ_1}$	3.85	3.85	2.77
	$e\phi_{WQ_2}/T_{eQ_2}$	3.82	3.84	2.66

Table 3 Discharge parameters for simulations with diferent SEE models and $\alpha_{B1} = 15$ deg. The different SEE models to be compared are identified by the superscript over the secondary electron types considered for the simulation: a corresponds to the SEE model defined in Section II and b uses the SEE model from Ref. [24].

realistic model of Ref. [24]. For the sake of illustration, results are presented for an scenario with $\alpha_{B1} = 15$ deg., although it has been checked that the main conclusions extracted here also apply to other magnetic magnetic field configurations.

The SEE model of Ref. [24] can include TS and NTS electrons; whereas the simple SEE model proposed in Section II considers only the emission of TS electrons. Then, the first comparison to be made aims to check whether TS electron emission is well characterized by the simple law of Eq. (3). As shown in Fig. 9 and Table 3 simulation results yield almost identical results; thus, suggesting that, for the range of electron impact energies in our simulations, the effect of TS electrons is well captured by the simple model.

Then, the effect of NTS electrons is addressed. Simulation results indicate that radial profiles of the main macroscopic magnitudes are weakly affected when non-true-secondaries are included. This is because, even if $\bar{n}_s$ is larger than in cases considering only TS, it is still small compared to $\bar{n}_e$. The main differences are found in wall interaction parameters, summarized in Table 3. The SEE yield grows from $0.21 - 0.28$ to $0.80 - 0.86$. However, it is still far from the charge saturation limit, estimated at $\langle \delta_s \rangle \sim 0.98$. The TS emission yield does not change significantly, since $\langle \mathcal{E}_e^{(tw)} \rangle$ does not experience major changes. Among NTS, backscattered electrons are dominant. Conversely to TS, which are emitted at an average energy of 2 eV, the emission energy of NTS depends on the energy of the wall impacting electron. This makes the mean electron emission energy, $\langle \mathcal{E}_e^{(fw)} \rangle$, grow from 2 to 8 eV. Since some of the electrons reaching the wall are reflected back, the VDF tails are less depleted in simulations including NTS than in previous simulations, where all the electrons reaching the walls are collected. This increases temperature slightly, reduces the anisotropy and leads to higher values of σ_{rp} and Θ. Even if σ_{rp} is higher, simulations including NTS electrons exhibit a lower potential fall across the sheath. In non-dimensional form, $e\phi_{WQ}/T_{eQ}$ decreases from $3.66 - 3.85$ to $2.66 - 2.77$ due to the effect of $\langle \delta_s \rangle$.

VIII. Conclusion and future work

The 1D radial kinetic model of the acceleration region of a HET discharge, developed in previous works [1–3], has been used to assess the effect of different magnetic configurations on plasma wall interaction. PIC results indicate a lower depletion of the electron VDF in those scenarios featuring an oblique magnetic field; thus, suggesting an enhanced

transfer of electrons between v_r and v_z regions. This induces a reduction in anisotropy, which agrees with previous observations by Miedzik et al. [15]. Macroscopic parameters, coming from the integration of the species VDF, are also affected in oblique magnetic field scenarios. It was found that this behavior is non-symmetric for convex ($\alpha_{B1} > 0$) and concave ($\alpha_{B1} < 0$) magnetic configurations. In particular, for $\alpha_{B1} > 0$, particle losses to the wall are promoted, the electron density remains rather uniform and significant electric potential gradients can be found in the bulk plasma region. On the other hand, for $\alpha_{B1} < 0$, particle losses decrease, large radial variations of electron density are found and the electric potential is almost flat, excluding the sheath regions close to the walls.

The analysis of the radial momentum equation explains the reason behind the relative shapes of n_e and ϕ depending on the convexity of the magnetic field lines. A new contribution due to the presence of an axial magnetic field appears in the radial electron momentum equation, which now becomes a balance among pressure, electric and magnetic force contributions. The pressure force tends to expands the electron fluid while the electric force tries to confine it. Conversely, the magnetic force changes sign with α_{B1}, so it is an outwards force for $\alpha_{B1} > 0$ and an inwards one for $\alpha_{B1} < 0$. The analysis of kinetic results shows that, for $\alpha_{B1} > 0$, the magnetic force, which tries to expand the fluid, is compensated by the electric force and the pressure force contribution remains small. For $\alpha_{B1} < 0$ the magnetic force, attempting to confine the electrons, is balanced by the pressure force and the electric force remains small in the bulk region.

To further clarify these results and how the electron fluid arranges this balance for different magnetic field incidence angles, a simplified fluid model is proposed and analyzed. Such model is validated against kinetic results and it has been confirmed to keep the essential fluid dynamic aspects of the plasma discharge. The fluid model provides valid solutions imposing the classical sonic ion flow condition at the sheath edge for $\alpha_{B1} < 0$ and small positive values of α_{B1}. However, beyond a certain value of α_{B1}, this boundary condition can no longer be imposed; instead, ions must reach the sheath edge at a supersonic speed. In such parametric region the ion radial velocity becomes linear and the sonic transition occurs within the quasi-neutral plasma region.

Asymmetries in the discharge are reduced in scenarios with an oblique magnetic field. Additionally, the replenishment parameter σ_{rp} grows significantly, in accordance with the computed shapes of the electron VDF. The non-dimensional sheath potential drop $e\phi_{WQ}/T_{eQ}$ incrases consistently, mainly as a consequence of the variations in σ_{rp}.

True secondary electron emission is well approximated by Eq. (3), yielding identical results to those obtained by more realistic and complex models. Non-true-secondary electrons have a weak influence on the main discharge features and affect only wall interaction parameters. In particular, $\langle \mathcal{E}_e^{(tw)} \rangle$, σ_{rp} and Θ report higher values since some of the electrons reaching the walls are reflected.

The simulations analyzed in this work disregards the effect of anomalous electron transport, although a previous article [1] showed that it affects several discharge parameters. Preliminary studies confirm that the main conclusions and trends extracted here remain valid in scenarios including anomalous transport. However, those cases are less affected by the magnitude of α_{B1}. This can be explained due to the important increase in T_e as a consequence of anomalous scattering events. The simplified fluid model condenses the oblique magnetic field effect in the non-dimensional parameter F. This parameter is proportional to $\tan \alpha_{B1}$ and inversely proportional to T_e. Thus, this simplified model tells us that, as long as $\alpha_{B1} \neq 0$, increasing T_e has the same effect on the plasma discharge as decreasing α_{B1}.

The analysis presented here covers symmetric magnetic configurations. However, we expect to extend this work to non-symmetric configurations as well, with $\alpha_{B1} \neq -\alpha_{B2}$. Finally, complex topologies, large incidence and wall parallel magnetic fields, in which axial dynamics are expected to play a major role, will be investigated using a 2D radial-axial PIC model, which will extend the simulation capabilities.

Acknowledgments

This work was funded mainly by Project PID2019-108034RB (Spain's National Research and Development Plan). Additional support came from the PROMETEO-CM project, Grant number Y2018/NMT-4750 (Comunidad de Madrid/FEDER/FSE).

References

[1] Marín-Cebrián, A., Domínguez-Vázquez, A., Fajardo, P., and Ahedo, E., "Macroscopic plasma analysis from 1D-radial kinetic results of a Hall thruster discharge," *Plasma Sources Science and Technology*, Vol. 30, No. 11, 2021, p. 115011. https://doi.org/10.1088/1361-6595/ac325e, URL https://doi.org/10.1088/1361-6595/ac325e.

[2] Domínguez-Vázquez, A., Taccogna, F., and Ahedo, E., "Particle modeling of radial electron dynamics in a controlled discharge of a Hall thruster," *Plasma Sources Science and Technology*, Vol. 27, No. 6, 2018, p. 064006.

[3] Domínguez-Vázquez, A., Taccogna, F., Fajardo, P., and Ahedo, E., "Parametric study of the radial plasma-wall interaction in a Hall thruster," *Journal of Physics D: Applied Physics*, Vol. 52, No. 47, 2019, p. 474003. https://doi.org/10.1088/1361-6463/ab3c7b, URL https://doi.org/10.1088%2F1361-6463%2Fab3c7b.

[4] Kaganovich, I., Raitses, Y., Sydorenko, D., and Smolyakov, A., "Kinetic effects in a Hall thruster discharge," *Physics of Plasmas*, Vol. 14, 2007, p. 057104.

[5] Taccogna, F., Schneider, R., Longo, S., and Capitelli, M., "Kinetic simulations of a plasma thruster," *Plasma Sources Science and Technology*, Vol. 17, No. 2, 2008, p. 024003.

[6] Linnell, J. A., and Gallimore, A. D., "Internal plasma potential measurements of a Hall thruster using plasma lens focusing," *Physics of Plasmas*, Vol. 13, No. 10, 2006, p. 103504.

[7] Hofer, R., Goebel, D., Mikellides, I., and Katz, I., "Magnetic shielding of a laboratory Hall thruster. II. Experiments," *Journal of Applied Physics*, Vol. 115, No. 4, 2014, p. 2008.

[8] Chodura, R., "Plasma-wall transition in an oblique magnetic field," *Physics of Fluids*, Vol. 25, 1982, pp. 1628–1633.

[9] Riemann, K., "Theory of the plasma-sheath transition in an oblique magnetic field," *Contributions to Plama Physics*, Vol. 34, 1994, pp. 127–132.

[10] Keidar, M., and Beilis, I. I., "Sheath and boundary conditions for plasma simulations of a Hall thruster discharge with magnetic lenses," *Applied Physics Letters*, Vol. 94, No. 19, 2009, p. 191501.

[11] Brieda, L., and Keidar, M., "Plasma-wall interaction in Hall thrusters with magnetic lens configuration," *Journal of Applied Physics*, Vol. 111, No. 12, 2012, p. 123302.

[12] Hagelaar, G., Bareilles, J., Garrigues, L., and Boeuf, J., "Two-dimensional model of a stationary plasma thruster," *Journal of Applied Physics*, Vol. 91, No. 9, 2002, pp. 5592–5598.

[13] Mikellides, I. G., Katz, I., Hofer, R. R., and Goebel, D. M., "Magnetic shielding of a laboratory Hall thruster. I. Theory and validation," *Journal of Applied Physics*, Vol. 115, No. 4, 2014, p. 043303.

[14] Zhou, J., "Modeling and simulation of the plasma discharge in a radiofrequency thruster," Ph.D. thesis, Universidad Carlos III de Madrid, Leganés, Spain, 2021.

[15] Miedzik, J., Barral, S., and Daniłko, D., "Influence of oblique magnetic field on electron cross-field transport in a Hall effect thruster," *Physics of Plasmas*, Vol. 22, No. 4, 2015, p. 043511.

[16] Nanbu, K., "Probability theory of electron-molecule, ion-molecule, molecule-molecule, and Coulomb collisions for particle modeling of materials processing plasmas and cases," *IEEE Transactions on plasma science*, Vol. 28, No. 3, 2000, pp. 971–990.

[17] Nanbu, K., "Simple method to determine collisional event in Monte Carlo simulation of electron-molecule collision," *Jpn. J. Appl. Phys.*, Vol. 33, No. 8, 2000, pp. 4752–4753.

[18] Surendra, M., Graves, D. B., and Morey, I. J., "Electron heating in low-pressure rf glow discharges," *Appl. Phys. Lett.*, Vol. 56, No. 11, 1990, pp. 1022–1024.

[19] Nanbu, K., "Theory of cumulative small-angle collisions in plasmas," *Phys. Rev. E*, Vol. 55, No. 4, 1997, pp. 4642–4652.

[20] Nanbu, K., and Yonemura, S., "Weighted particles in Coulomb collision simulations based on the theory of a cumulative scattering angle," *J. Comput. Phys.*, Vol. 145, 1998, pp. 639–654.

[21] Bobylev, A. V., and Nanbu, K., "Theory of collision algorithms for gases and plasmas based on the Boltzmann equation and the Landau-Fokker-Plack equation," *Phys. Rev. E*, Vol. 61, No. 4, 2000, pp. 4576–4586.

[22] Wang, C., Lin, T., Caflisch, R., Cohen, B. I., and Dimits, A. M., "Particle simulation of Coulomb collisions: comparing the methods of Takizuka & Abe and Nanbu," *J. Comput. Phys.*, Vol. 227, No. 9, 2008, pp. 4308–4329.

[23] Ahedo, E., Gallardo, J., and Martínez-Sánchez, M., "Effects of the radial-plasma wall interaction on the axial Hall thruster discharge," *Physics of Plasmas*, Vol. 10, No. 8, 2003, pp. 3397–3409.

[24] Furman, M. A., and Pivi, M. T. F., "Probabilistic model for the simulation of secondary electron emission," *Phys. Rev ST Accel. Beams*, Vol. 5, No. 12, 2002, p. 124404.

[25] Wang, H., Campanell, M. D., Kaganovich, I. D., and Cai, G., "Effect of asymmetric secondary emission in bounded low-collisional E× B plasma on sheath and plasma properties," *Journal of Physics D: Applied Physics*, Vol. 47, No. 40, 2014, p. 405204.